Available online at www.sciencedirect.com

SciVerse ScienceDirect

Acta Materialia 60 (2012) 2471–2478

Acta MATERIALIA

www.elsevier.com/locate/actamat

Strain-hardening in submicron silicon pillars and spheres

Douglas D. Stauffer [a,*], Aaron Beaber [a], Andrew Wagner [a], Ozan Ugurlu [b], Julia Nowak [c], K. Andre Mkhoyan [a], Steven Girshick [d], William Gerberich [a]

[a] Chemical Engineering & Materials Science, University of Minnesota, United States
[b] Characterization Facility, University of Minnesota, United States
[c] Hysitron Inc., Minneapolis MN, United States
[d] Mechanical Engineering, University of Minnesota, United States

Received 6 August 2011; received in revised form 16 October 2011; accepted 22 October 2011
Available online 16 February 2012

Abstract

Measurements of submicron spheres and pillars of silicon single crystals have exhibited a strain-hardening capacity equal to or greater than their metallic counterparts. Stress–strain characteristics are reported for diameters ranging from 40 to 400 nm. Evaluations were performed with nanoindentation-based atomic force, scanning and transmission electron microscopies. Values of strain-hardening exponents up to unity in nanospheres are attributed to a size effect variation on the rate of increase of contact area with deformation. A surface-mediated dislocation nucleation concept is shown to be consistent with length scale effects partially modified by geometry as well as size. It is proposed, but not proven, that the modification relates to greater constraint in compact spheres as opposed to tall pillars.

Keywords: Nanoparticle compression; Plasticity; Silicon

1. Introduction

For devices in switches requiring electrical contacts or for microelectromechanical systems devices subjected to repeated stress, strain-hardening capacity can be critical. There has been a lack of understanding of nanoscale strain hardening due to the difficulties in performing and interpreting such experiments. Additionally, there may be a perception from some studies on face-centered cubic (fcc) materials that little strain hardening exists [1–4], although other more recent experiments report high hardening in both fcc [5–8] and body-centered cubic (bcc) materials [9–12]. For other crystal structures such as zinc blendes or diamond cubic, Rabier and Demenet [13] demonstrated substantial hardening for compression under confined pressure. Additionally, a decade of examination of submicron silicon nanospheres in the 40–400 nm range shows that even very small silicon single crystals undergo strain hardening [14,15]. This is a pivotal test case for our hypothesis that materials in crystalline form, both metals and ceramics, can possess strain-hardening capacity in compression. Silicon is known to exhibit more plasticity than oxides and carbides during nanoindentation, but less than metals and intermetallics. For a material with yield stresses in the GPa range due to the high Peierls barrier [16,17], it is difficult to conceive of very large strain-hardening capacity. Observations in both spheres and pillars refute this misconception.

In the following, experimental evaluations of nanospheres and nanopillars will be described, and strain-hardening exponents >0.3 demonstrated. In the case of the more confined spheres, values near unity arise. Experimentally, the analysis of nanopillars is straightforward but spheres are analyzed in two ways due to strain gradients arising from the spherical geometry. Single-crystal silicon pillars with diameters of 160–415 nm and spheres with diameters of 39–338 nm are described [15]. Examples of the plastic deformation which may arise in these samples are shown in Fig. 1. An ad hoc theoretical application of surface-mediated dislocation nucleation is then applied to

* Corresponding author. Tel.: +1 612 624 0515.
E-mail address: stauffer@umn.edu (D.D. Stauffer).

1359-6454/$36.00
doi:10.1016/j.actamat.2011.10.045

both spheres and pillars. Size effects are observed wherein the magnitude of strain-hardening exponents changes with length scale due to relative geometry and constraint effects.

2. Experimental procedures

Experimental analysis is complex for spheres due to the small initial contacts which produce large stresses at the top and bottom of the spheres compressed by a sapphire substrate and a large radius diamond tip. The deposition by hypersonic plasma deposition [18] and focused nanoparticle beam [19] and analysis of such spheres is described in more detail elsewhere [20]. Originally, [14,15] these spheres were compressed with a Hysitron Triboscope™ mounted on a Digital Instruments™ atomic force microscope (Fig. 2). Later, similar experiments were repeated with in situ imaging, using a PicoIndenter™ inside a JEOL™ or FEI-T12™ transmission electron microscope. For more details, see Refs. [21,22]. The atomic force microscopy (AFM) system, run in load-controlled feedback mode, allowed investigation of smaller nanoparticles than in transmission electron microscopy (TEM) due to line-of-sight requirements. As discussed elsewhere [15], repeated runs on the same nanoparticle could be obtained with total strains of up to approximately 0.2 for individual runs and a summation of up to 0.5, as shown in Fig. 2 for a 43.6 nm diameter sphere. As the total strain could be quite large, flattening of the sphere needed to be considered. Initially,

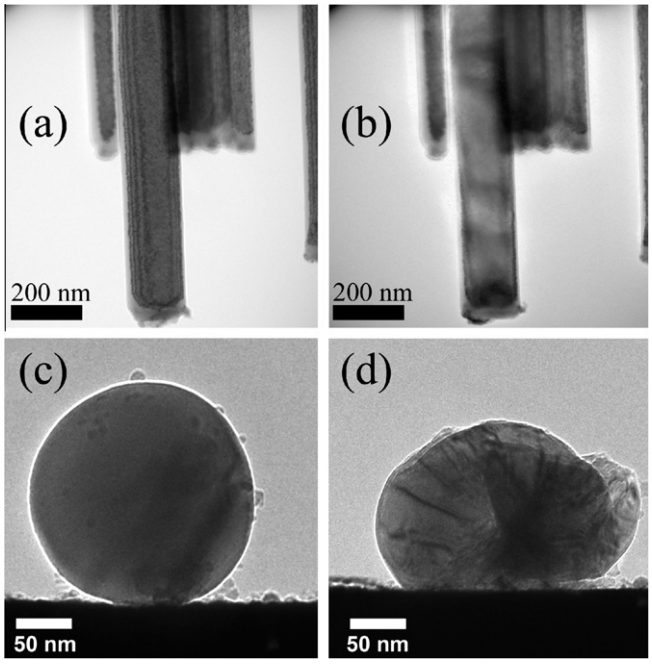

Fig. 1. TEM micrograph examples of in situ work-hardened Si nanopillars (a, b) and spheres (c, d). The undeformed 180 nm Si pillar of (a) was compressed three times to a strain of less than 5% (b). The Au cap, from the VLS growth, was removed prior to indentation. The Si sphere (c) was compressed once (d).

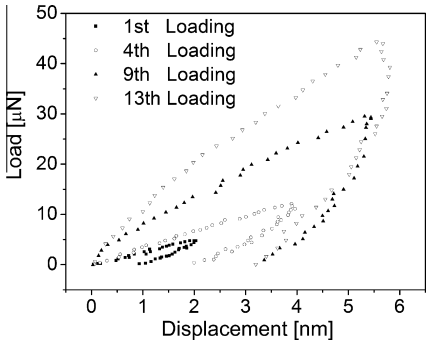

Fig. 2. Load–depth curves for repeat loading of a 43.6 nm sphere, where loading was done with a Triboscope system under load control.

the contact areas were small, generating large contact stresses at very small loads. To quantify the stresses, the geometric contact radius was found from

$$a = \left[\delta r - \frac{\delta^2}{4}\right]^{1/2}, \tag{1}$$

where δ is the total displacement divided equally into the top and bottom of the sphere of radius, r. The geometric contact consideration is due to elastic and plastic deformation. Given that the region directly under the contacts is undergoing severe plastic deformation, additional steps to evaluate the global strain hardening were required, particularly for repeat runs. First, for any repeat run the initial contact area increases due to the residual plastic deformation from the previous run(s), as measured by AFM and described elsewhere [14,15]. Second, the initial strain for any given run started from zero in the unloaded state as required. To obtain a more representative equivalent stress, a conversion of initial radius of the sphere, r_0, to an effective radius, r_{eff}, was needed. This was accomplished using constancy of volume, assuming an increasing pancaking of the sphere to more closely resemble a right cylinder. A uniform stress of a right cylinder with an equivalent volume was found from:

$$\frac{4}{3}\pi r_0^3 = \pi r_{eff}^2 (h_0 - \delta), \tag{2}$$

where h_0 was taken to be equal to the original diameter of the sphere, $h_0 = 2r_0$, giving:

$$r_{eff} = 1.155 r_0 \left[\frac{r_0}{2r_0 - \delta}\right]^{1/2}. \tag{3}$$

See Fig. 3. Stresses were evaluated in two ways, using the equivalent right cylinder with $A = \pi r_{eff}^2$, which gives an average stress for an equivalent volume. A harmonic mean with a contact stress was based on Eq. (1), and the average stress obtained from Eq. (3). The harmonic mean stress considers the deformed sphere as a layered structure, with stresses taken as layers of highly deformed regions at the contact based upon Eq. (1) and a more nearly average area radius from Eq. (3). This concept of a layered structure, as observed by TEM contrast differences [22] gives

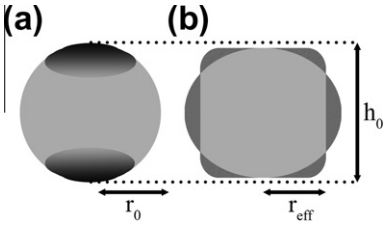

Fig. 3. Schematic representation of (a) the harmonic mean approximation in a sphere, where a bilayer system is used to model the damage region in the sphere, and (b) the right-cylinder approximation.

rise to a harmonic mean stress as used by Hill for composite structures [23]. This gave a stress intermediate to those using Eqs. (1) and (3) with the harmonic mean given by:

$$\sigma_m = \frac{2}{\frac{1}{\sigma_c} + \frac{1}{\sigma_{cyl}}}. \tag{4}$$

Here σ_c is the contact stress using Eq. (1) and σ_{cyl} is the equivalent stress of a right cylinder using Eq. (3). The harmonic mean stress is the Voigt average which represents a lower bound. A similar set of procedures for strains took the strain in the two contact regions, after Tabor [24], to be:

$$\varepsilon_c = 2\left\{0.2\left(\frac{a}{r}\right)\right\}, \tag{5}$$

and took the average strain throughout to be:

$$\varepsilon_d = \frac{\delta}{d}. \tag{6}$$

Here the extra factor of 2 in Eq. (5) is due to strain on both the top and the bottom. Coupling the Tabor strain with the global estimate, Eqs. (5) and (6), gave a harmonic mean strain given by:

$$\varepsilon_m = \frac{2}{\frac{1}{\varepsilon_c} + \frac{1}{\varepsilon_d}}. \tag{7}$$

Two types of stress–strain representations used Eqs. (3) and (6) for the right-cylinder approximation and Eqs. (4) and (7) for the harmonic mean. The strain-hardening behavior was found from true stress–true strain plots in compression:

$$\sigma_T = \sigma(1+\varepsilon); \quad \varepsilon_T = \ln(1+\varepsilon), \tag{8}$$

keeping in mind that, in compression, strains are negative. From such plots, the strain-hardening exponents, n, were determined from the power-law equation, with the coefficient, k, giving:

$$\sigma_T = k\varepsilon_T^n. \tag{9}$$

Using Eq. (9), strain-hardening exponents were also determined for columns of nanopillars loaded in compression. Only a few of these data were available with two representing pillars prepared by focused-ion-beam (FIB) machining, and others representing growth by a vapor–liquid–solid (VLS) process where the Au growth catalyst was removed using a commercially available chemical etchant, Transene, TFA. The FIB samples had a small taper [25] but the VLS samples were relatively straight-sided.

In creating the stress–strain plots, it is emphasized that the load–displacement curves were only analyzed up to the point of fracture. Signatures of either load drops for the in situ TEM experiments or height image drops during AFM scans, as explained elsewhere [14,15], signified fracture. Data were only used up to the point of fracture.

3. Results

Using true stress–true strain, for two repeat ex situ loadings of spheres in Fig. 4, strain-hardening exponents are reported for repeat runs on five nanoparticles in Tables 1a–c. These were based on the right-cylinder method. Apart from the smallest nanospheres, there appears to be a strong increase in strain-hardening exponent with increased sphere diameter. Average values increased by a factor of 3 from 0.25 to 0.75 as size increased from 43.6 to 92.7 nm.

Additionally, single runs were generally conducted to a strain of 0.4, calculated by Eq. (6), for eight spheres in the size range 60–340 nm. These tests were compressed with the in situ system, with all except the 63 nm sphere tested in displacement control. The 63 nm sphere was tested in open loop (OL). Examples for four of these runs, see Fig. 5, show a similar trend of increasing stress as size decreases. Here, for stresses defined by the right-cylinder method, there was nearly a factor of 6 increase in average stress as size decreased. This is larger than what might be expected as addressed in the discussion below. With the exception of the OL tested sphere, a factor of 4 increase in sphere diameter produced a factor of 4 increase in strain-hardening exponent (Table 1b and Fig. 5). To double check these estimates of strain hardening, the layered structure of the harmonic mean approach of Eqs. (4) and (7) was also used to determine n. Four true stress–strain

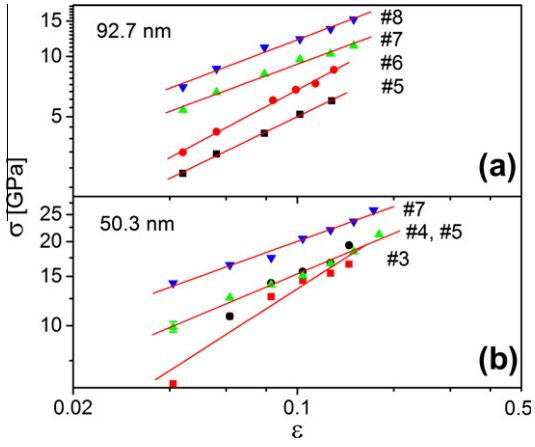

Fig. 4. True stress–true strain for two spheres tested in the Triboscope system, where the harmonic mean approximation was used to determine the stress. Work hardening, due to cumulative damage, can be seen as increasing stress for a given strain as the run number increases. Strain-hardening exponents are given in Table 1a. Typical error bars due to instrument noise floors as shown outside a given data point are often within the symbol at higher stresses and strains.

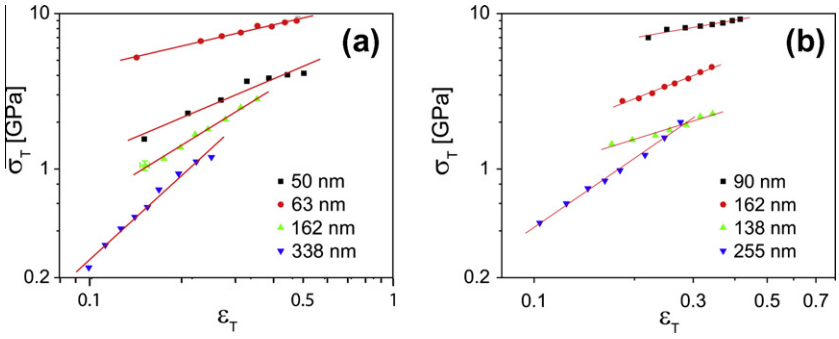

Fig. 5. (a) A comparison of the true stress–true strain plots for the first compression of individual spheres, tested in load control. Stresses here are determined using the right-cylinder approximation. (b) A comparison of the true stress–true strain plots for the first compression of individual spheres determined using the harmonic mean approximation. With respect to the model curves, it is emphasized that the two curves represented are due to the Schmid factor extremes chosen rather than any clustering of data to a particular orientation. Typical error bars due to instrument noise floors shown outside a given data point are often within the symbol at higher stresses and strains.

plots (Fig. 5b) can be compared to the data for the 90 and 162 nm spheres of Fig. 5a, with similar strain-hardening exponents.

To check the validity of using indirect calculations of strain-hardening exponents, direct measurement of the contacting radius was attempted from individual movie frames on two spheres, one of 138 nm and another of 338 nm diameter. Most importantly, the limited space in which one can view the compression inhibited our ability to make precise measurements given the possibility of tilt or parallax. Nevertheless, using Eqs. (4) and (7) to determine strain-hardening exponents, it was found that n for the largest sphere was 12.7% smaller and n for the smaller one 6.7% larger than those based only on calculations.

There was one major discrepancy when comparing the 63 and 93 nm diameter spheres tested by AFM compared to the 63 and 90 nm spheres tested by TEM. The AFM-tested strain-hardening exponents were about 50% higher. Although unproven, the only major difference appears to be the electron beam effect which can produce radiation-enhanced dislocation glide. Even though the transmission electron microscope was only operated at 120 keV, it is conceivable that more rapidly moving dislocations in the in situ TEM experiments may lead to dislocation rearrangement or egress from a given diameter sphere, which in turn affects strain hardening.

Turning to the micropillars, the relatively uniform diameters simplified the stress analysis and only load/area and displacement/length were used to analyze engineering stress–strain, followed by Eq. (8) to obtain the true stress–true strain. Six pillars were analyzed for their strain-hardening characteristics. The 180 nm diameter pillar was repeatedly compressed to small plastic strains, of the order of 1–2%, to stresses between 2 and 4 GPa (Fig. 6a). Beyond this there was clearly an onset of bending. Four other pillars, two each of $\langle 1\,0\,0\rangle$ and $\langle 1\,1\,1\rangle$ orientations, were singly compressed (Fig. 6b). In general the strain-hardening exponent increased with repeat runs, but seemed to decrease with increasing pillar size. This decrease appears inconsistent with the sphere size effect which showed strain hardening increasing with increasing sphere size (Table 1c). These differences are discussed, after some theoretical considerations, in the following sections.

4. Theoretical considerations

Due to the apparently large variations in strain-hardening exponents in Tables 1a–c, it was important to provide an analysis as to why this size-dependent effect might arise. Two obvious variables are dislocation nucleation limited and dislocation motion limited behavior. As size decreases, the number of nucleation sites decreases. Similarly, a decreased size could limit the mean free path of dislocation motion if there is any constraint at the surface. Constrained flow could possibly increase both strength and strain hardening. With reliable true stress–true strain behavior from in situ TEM and SEM methods analogous to those pioneered by others [26–31], the experimental results can be compared to a proposed first-order model as detailed in the Appendix (Supplementary information). In terms of the available surface sites, and assuming that the activation of a surface site is proportional to a stress, the strain-hardening exponent is proposed to be:

$$n = \text{const.} \times \frac{\text{no. of surface sites}}{\text{unit area}} \times \frac{\sigma}{\mu}, \tag{10}$$

with the stress, σ, normalized by the shear modulus, μ. As seen in the Appendix, constants of $\beta\gamma$ times a Burgers vector, b, as related to contact surface sites can be combined with a Hall–Petch representation of stress to give:

$$n = \frac{\pi k_y d^{1/2} \cos\phi \cos\lambda}{\beta\gamma b\mu}, \tag{11}$$

with $\cos\phi\cos\lambda$ resolving the shear stress. As dislocations are either non-existent or contribute little to strain hardening below a cut-off diameter, d_0, this is included by modifying n to be:

$$n = \frac{\pi k_y (d - d_0)^{1/2} \cos\phi \cos\lambda}{\beta\gamma b\mu}. \tag{12}$$

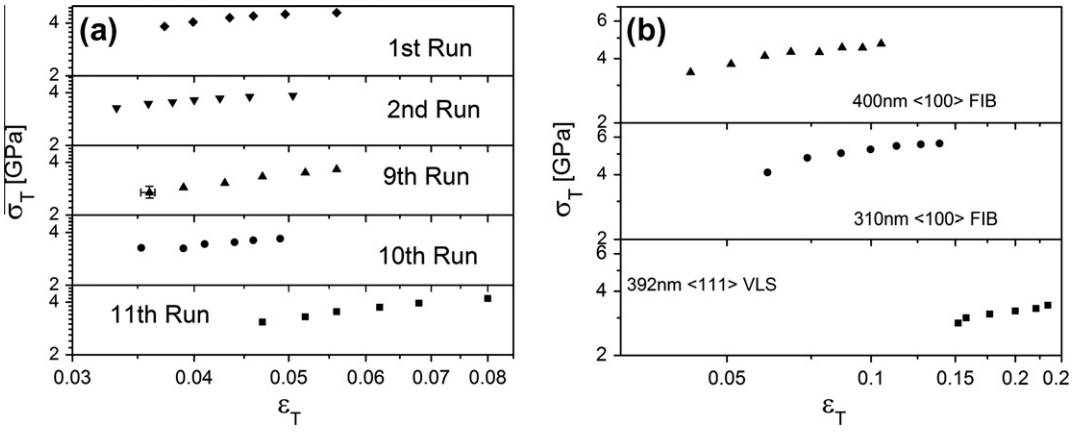

Fig. 6. True stress–true strain for (a) repeat compression for a 160 nm ⟨1 1 1⟩-oriented Si pillar, grown by VLS—bending of the pillars was observed at larger strains; and for (b) three FIB-cut Si towers. Two towers are oriented in the ⟨1 0 0⟩, and one in the ⟨1 1 1⟩. Values for the strain-hardening exponent are given in Table 1c. Typical error bars due to instrument noise floors as shown outside a given data point are often within the symbol at higher stresses and strains.

With $\beta\gamma$ defined, the strain-hardening results can be compared for the deformed spheres using Eq. (12). However, the cylinders represent a different geometry. As with the spheres, it is assumed that the number of dislocation nucleation sites increases with stress, but with a different functionality (see Appendix for details). For cylinders, then, it is proposed that the strain-hardening exponent is given by:

$$n = \frac{\pi k_y d^{1/2} \cos\phi \cos\lambda}{16\beta\gamma b\mu\varepsilon^{1/2}}. \tag{13}$$

The somewhat smaller strain-hardening exponents in the pillars compared to the spheres is attributed to a less effective confinement in a tall cylinder, with a greater volume-to-surface ratio.

5. Discussion

It is important to demonstrate the differences in strain-hardening exponents for the two proposed methods, harmonic mean and right-cylinder averages, Eqs. (1)–(8). Qualitatively, the stress–strain plots appear similar (Fig. 5a and b) to those measured by TEM; a direct comparison of the exponents is shown in Fig. 7a. For both approaches, there is a strong increase in strain-hardening exponent with increasing sphere diameter. Both methods gave similar results for spheres less than 150 nm in diameter, but the harmonic mean approach consistently gave higher strain-hardening exponents at larger diameters. Further analysis used the simpler right-cylinder method.

Qualitatively, for both sets of sphere data, see Tables 1a and b, there is a large increase in n with sphere diameter, with the exception of two points (see Fig. 7b). This increase in n is considered to be due to the increase in dislocation nucleation rate in the larger spheres with increasing strain. It must be considered that since the activation area bears an inverse relationship to the applied stress, then as stress increases, more nucleation sites become available. This is coupled to the high stresses in the small spheres. However, these sites are rapidly exhausted in small spheres and the subsequent rate of hardening is much reduced. This is exacerbated by the confinement represented by the smaller spheres. The diameter is coupled to the length of the mean free path of dislocations due to the back-stress from dislocation interactions. This can prevent further dislocation nucleation in the smaller spheres. It is proposed that it is this combination of surface-mediated dislocation nucleation and confinement that leads to smaller increases in dislocation densities per unit strain and hence lower strain-hardening exponents. Clearly, confinement decreases in larger spheres and, coupled with increased contact area, the potential for dislocation nucleation increases with larger strains. As stated previously, this is somewhat offset by the elevated flow stresses in small spheres. Both of these features are embodied in Eq. (12).

The data intersects the theory through the activation area, A^*, as discussed following Eq. (A8). Since A^* is defined by V^* and $\beta\gamma$ can be defined for a given k_y, the only other unknown in Eq. (12) is d_0, a cut-off parameter. Here, a d_0 of 40 nm was chosen to fit the data and a k_y of 1 MPa m$^{1/2}$ was selected as it approximated the strength data of this investigation. With the two extremes of $\cos\phi\cos\lambda$ based on {1 1 1} slip and orientations of either ⟨1 0 0⟩ or ⟨1 1 1⟩, Eq. (12) was compared to data from Tables 1a and b in Fig. 7b. It can be seen that the strain-hardening exponents are at least qualitatively reproduced but that a discrepancy between the two loading methods results with the displacement control data favoring a theoretical fit of $\cos\phi\cos\lambda = 0.408$ and the load control data favoring a fit with $\cos\phi\cos\lambda = 0.272$. This is fortuitous, however, as the loading axis for all of these spheres is unknown. The two points furthest off either curve of Eq. (12) represent a 38.6 nm diameter sphere and the solid point one 63 nm in diameter. The latter, which was evaluated under OL conditions, appears to match the load control data better.

Next, consider the data of Table 1c and Fig. 6a and b for pillars. Because of prior bending in the previous runs,

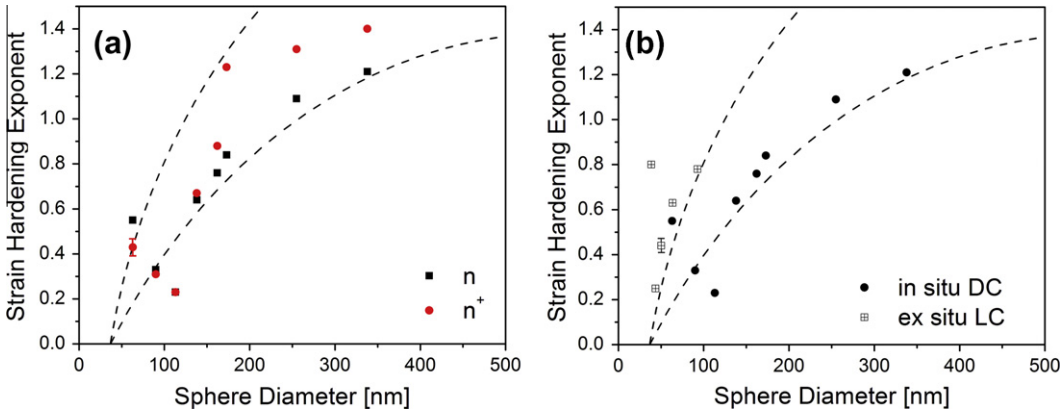

Fig. 7. (a) Strain-hardening exponent for the Si spheres plotted vs. the sphere diameter. Values calculated by the right-cylinder approximation (squares) are smaller than those using the harmonic mean approximation (circles), especially for larger diameters. (b) The strain-hardening exponents for the load-controlled data trend higher than the dashed lines, which are based on Eq. (12) using large variations in $\cos\phi\cos\lambda$. Typical error bars due to instrument noise floors as shown outside a given data point are often within the symbol at higher stresses and strains. Error bars on sphere diameter are within the data points.

Table 1a
Strain-hardening exponents, measured for each run for multiply loaded Si spheres with diameters ranging from 38.6 to 92.7 nm. A Triboscope/AFM system was used in load-controlled mode for these compressions. The strain-hardening exponents were calculated using the right-cylinder approximation.

Sphere diameter (nm)	Test method	Run #/strain hardening exponent, n						$\bar{n}$
38.6	LC	2/0.79	5/0.90	7/0.94	9/0.75	12/0.78	15/0.66	0.80 ± 0.14
43.6	LC	2/0.23	3/0.21	4/0.15	5/0.38	6/0.29		0.25 ± 0.13
50.3	LC	2/0.41	3/0.49	4/0.49	5/0.44	7/0.39		0.44 ± 0.05
63.5	LC	2/0.62	3/0.63	4/0.64	5/0.64	6/0.63		0.63 ± 0.02
92.7	LC	3/0.81	4/0.81	5/0.75	6/0.77	7/0.69	8/0.65	0.75 ± 0.10

LC = load control.

Table 1b
Strain-hardening exponents, measured for each run for Si spheres singly compressed primarily in displacement control. Here, an in situ PicoIndenter was used to perform the compressions. Exponents are given for each of the two analysis methods, i.e. harmonic mean and right-cylinder approximations.

Sphere diameter (nm)	Test method	n (Right cylinder)	n (Harmonic mean)	$\bar{n}$
63	Open Loop	0.55	0.43	0.49
90	DC	0.33	0.31	0.32
113	DC	0.23	0.23	0.23
138	DC	0.64	0.67	0.66
162	DC	0.76	0.88	0.82
173	DC	0.84	1.23	1.04
255	DC	1.09	1.31	1.20
338	DC	1.21	1.40	1.31

stresses to achieve the same 5% strain progressively decreased from 4.5 to 3.3 GPa. Note that the aspect ratio, i.e. height to diameter, was closer to 5:1 for the smallest diameter pillars. For reliable measures of strain hardening, additional experiments will be required for aspect ratios closer to 3:1.

There are literature data for pillars of this aspect ratio for somewhat larger MgO single crystals. As shown in the Appendix, n values ranged from 0.2 to 0.4 consistent with the reported measurements here for larger-diameter silicon nanopillars. For the four larger-diameter pillars with smaller aspect ratios, the bending is sufficiently suppressed that reasonable strain-hardening exponents of 0.3 ± 0.08 are found for the two pillar orientations of $\langle 1\,0\,0\rangle$ and $\langle 1\,1\,1\rangle$. As the average pillar size was 380 nm, this result compares to a measured strain-hardening exponent of greater than unity for a corresponding diameter sphere. This may be qualitatively understood considering the relative confinement and increased dislocation activity for the sphere compared to the pillar. How do these differences compare to what might be expected from Eqs. (11)–(13)? The average strain for the four largest samples is 0.109, giving $\varepsilon^{1/2}$ equal to 0.33. Since $4\varepsilon^{1/2}$ is little different from unity it appears that the strain-hardening exponent for comparable diameter pillars could be nearly a factor of 4 smaller than the spheres as observed for the 300–400 nm size range.

Finally, it is probably that some of the larger spheres, but not the pillars, exhibit the diamond cubic to β-Sn

Table 1c
Determination of strain-hardening exponents of Si pillars using the in situ SEM and TEM PicoIndenters for ⟨111⟩- and ⟨100⟩-oriented pillars operated in displacement control.

Pillar diameter (nm)	Test method	n	Orientation	Notes
180	DC	0.415	⟨111⟩	Plastic bending or
200	DC	0.706	⟨111⟩	buckling suggested
310	DC	0.316	⟨100⟩	FIB cut
392	DC	0.355	⟨111⟩	VLS grown
400	DC	0.293	⟨100⟩	FIB cut
415	DC	0.220	⟨111⟩	VLS grown

DC = displacement control, FIB = focused ion beam, VLS = vapor–liquid–solid.

(silicon I→II) phase transformation on loading. This usually manifests itself by a pop-in (loading) or pop-out, or knee, in the load–displacement curve (unloading) [33,34]. In a separate study of nano- and submicron-spheres, it is shown that there is a size transition in behavior from deformation of microspheres to nanospheres [35]. Below approximately 100 nm there is no phase transformation, while for larger microspheres a phase transformation occurs. Perhaps appropriate to this study, Gogotsi et al. suggest that "indentation-induced metallization (Silicon II) ... is accompanied by confined plastic flow ... in order to partially accommodate high strains in the surrounding material."[29] In fact some characteristic pop-outs, but mostly a knee in the unloading curve of larger nanospheres, have been observed, which is often cited as a signature of the phase transformation [36]. Future work should address whether it is dislocation plasticity, phase transformation or a combination of the two which results in the large jump in strain-hardening exponent in the 100–150 nm diameter regime.

Refinement of such approaches for both geometries requires discretized dislocation dynamics, computational approaches using molecular dynamics and detailed electron microscopy studies using in situ deformation techniques.

Additionally, one would expect a transition from a primary plastic regime to crack tip blunting or mixed mode regime, and finally to a bulk-type behavior. In fact, this is what is observed by Östlund et al. in Si pillars as the diameters increase to 400 nm [25].

6. Summary

Experimentally, deformation of single-crystal Si nanospheres and submicron pillars have been measured in compression. Considerable plasticity is evident, with plastic strains approaching 0.5 for spheres. As observed by TEM and AFM with in situ loading devices, considerable strain hardening is also observed. Strain-hardening exponents ranging from 0.2 to 1 are found. Size dependence increases as the square-root of the sample diameter, which can be explained by nucleation source-limited and flow-limited theory. For a given diameter in the range of 200–400 nm, spheres have a hardening exponent approximately three times larger than that of pillars with a 4:1 aspect ratio, a finding that can be explained by the relative confinement and contact areas in pillars compared to spheres.

Acknowledgements

The authors would like to acknowledge the Abu Dhabi-Minnesota Institute for Research Excellence a partnership with the Petroleum Institute, NSF/DMR- 0946337, and NSF/CTS-0506748 for funding. Some of the pillars described in this work were provided by Sergiy Krylyuk and Albert Davydov of the Metallurgy Division, MML at NIST Gaithersburg. D.S. and J.N. would additionally like to acknowledge Hysitron, Inc. Parts of this work were carried out in the Institute of Technology Characterization Facility, University of Minnesota, a member of the NSF-funded Materials Research Facilities Network.

Appendix A. Supplementary material

Supplementary data associated with this article can be found, in the online version, at doi:10.1016/j.actamat.2011.10.045.

References

[1] Uchic MD, Dimiduk DM, Florando JN, Nix WD. Science 2004;305:986.
[2] Volkert CA, Lilleodden ET. Philos Mag 2006;86:5567.
[3] Brinckmann S, Kim J-Y, Greer JR. Phys Rev Lett 2008:100.
[4] Bei H, Shim S, Pharr GM, George EP. Acta Mater 2008;56:4762.
[5] Shan ZW, Mishra RK ASAS, Warren OL, Minor AM. Nat Mater 2008;7:115.
[6] Kiener D, Grosinger W, Dehm G, Pippan R. Acta Mater 2008;56:580.
[7] Ng KS, Ngan AHW. Acta Mater 2008;56:1712.
[8] Frick CP, Clark BG, Orso S, Schneider AS, Arzt E. Mater Sci Eng A 2008;489:319.
[9] Greer JR, Nix WD. Appl Phys A: Mater Sci Process 2005;80:1625.
[10] Greer JR, Nix WD. Phys Rev B 2006;73:245410.
[11] Schneider AS, Kaufmann D, Clark BG, Frick CP, Gruber PA, Monig R, et al. Phys Rev Lett 2009;103:105501.
[12] Schneider A, Frick CP, Clark A, Arzt E. Mater Sci Eng A 2011;528:1540.
[13] Rabier J, Demenet JL. Phys Status Solidi (b) 2000;222:63.
[14] Gerberich WW, Mook WM, Perrey CR, Carter CB, Baskes MI, Mukherjee R, et al. J Mech Phys Solids 2003;51:979.
[15] Mook WM, Nowak JD, Perrey CR, Carter CB, Mukherjee R, Girshick SL, et al. Phys Rev B 2007;75:214112.
[16] Stach EA, Hull R. Appl Phys Lett 2001;79:335.
[17] Hull R, Bean JC, Peticolas LJ, Weir BE, Prabhakaran K, Ogino T. Appl Phys Lett 1994;65:327.
[18] Rao NP, Tymiak N, Blum J, Neuman A, Lee HJ, Girshick SL, et al. J Aerosol Sci 1998;29:707.

[19] Fonzo FD, Gidwani A, Fan MH, Neumann D, Iordanoglou DI, Heberlein J, et al. Appl Phys Lett 2000;77:910.
[20] Beaber AR, Qi L, Hafiz J, Heberlein J, Gerberich WW, Girshick S. Surface Coat Technol 2007:207.
[21] Nowak JD, Mook WM, Minor AM, Gerberich WW, Carter CB. Philos Mag 2007;87:29.
[22] Nowak JD, Beaber AR, Ugurlu O, Girshick SL, Gerberich WW. Scr Mater 2010;62:819.
[23] Hill R. Proc Roy Soc Lond 1952;A65:349.
[24] Tabor D. The hardness of metals. New York: Oxford Clarendon Press; 1951.
[25] Östlund F, Rzepiejewska-Malyska K, Leifer K, Hale LM, Tang Y, Ballarini R, et al. Adv Funct Mater 2009;19:2439.
[26] Gane N, Bowden FP. J Appl Phys 1968;39:1432.
[27] Gane N. Proc Roy Soc Lond A 1970;317:367.
[28] Lutwyche MI, Wada Y. Appl Phys Lett 1995;66:2807.
[29] Naitoh Y, Takayanagi K, Tomitori M. Surf Sci 1996;357–358:208.
[30] Wall MA, Dahmen U. Microsc Microanal 1997:3.
[31] Minor AM, Morris JJW, Stach EA. Appl Phys Lett 2001;79:1625.
[33] Rao R, Bradby JE, Ruffell S, Williams JS. Microelectr J 38:722.
[34] Juliano T, Gogotsi Y, Domnich V. J Mater Res 2003;18:1192.
[35] Beaber AR, Girshick S, Gerberich WW. A length scale dependent phase transformation in Si. 2011 TMS annual meeting & exhibition. San Diego, CA; 2011.
[36] Chrobak D, Tymiak N, Beaber AR, Ugurlu O, Gerberich WW, Nowak R. Nature Nanotechnol 2011;6:480.